ELSEVIER

Catalysis Today 59 (2000) 47–60

CATALYSIS TODAY

www.elsevier.com/locate/cattod

A critical evaluation of Navier–Stokes, boundary-layer, and plug-flow models of the flow and chemistry in a catalytic-combustion monolith

Laxminarayan L. Raja[a,*], Robert J. Kee[a], Olaf Deutschmann[b], Juergen Warnatz[b], Lanny D. Schmidt[c]

[a] *Division of Engineering, Colorado School of Mines, Golden, CO 80401, USA*
[b] *Interdisziplinaeres Zentrum fuer Wissenschaftliches Rechnen (IWR), Universitaet Heidelberg, 69120 Heidelberg, Germany*
[c] *Department of Chemical Engineering and Material Science, University of Minnesota, Minneapolis, MN 55455, USA*

Abstract

The objective of this paper is to evaluate three alternative formulations for simulating the steady-state flow and chemistry in a honeycomb channel for conditions that are typical of the catalytic combustion of natural gas. In developing simulation capabilities, it is important to understand the physical and computational accuracy that a model can deliver and the computational resources required to do so. Direct comparison of the solutions, using three different model formulations, reveal the range of validity of the various approximations. Computation times range from hours for the Navier–Stokes formulation to seconds for the plug-flow models.

Keywords: Catalytic combustion; Honeycomb monolith; Numerical modeling; Navier–Stokes; Boundary layer; Plug flow

1. Introduction

Catalytic combustion is emerging as a viable technology to achieve ultra-low emission of NO_x in applications like gas turbines for electric-power generation [1]. The combustor designs typically call for monolith systems that offer high catalyst area yet low pressure drop.

Design and control of honeycomb-type catalyst monoliths will be facilitated by the development and application of predictive models. All such models must consider heterogeneous chemical kinetics and transport, as well as possibly some homogeneous chemistry. Depending on the flow conditions, certain approximations and simplifications may be appropriate in representing the heat and mass transport. The most comprehensive models are based on solving the complete Navier–Stokes equations, considering both axial and radial mass, momentum, and energy transport. However, such models are computationally expensive, as well as being difficult to develop and often difficult to use. Plug-flow models, on the other hand, are relatively simple to write and easily solved on a personal computer. Since no diffusive terms remain, the plug-flow equations form a differential-algebraic-equation (DAE) initial-value problem for the axial variation of the mean species composition. An intermediate alternative is to base models on the boundary-layer equations, wherein axial (flow-wise) diffusive transport is neglected, but detailed transport to and from the channel walls is retained. These models represent a very significant

* Corresponding author.

0920-5861/00/$ – see front matter
PII: S0920-5861(00)00271-6

reduction in computational expense compared to a Navier–Stokes formulation but an increase in computational expense relative to the plug-flow model.

The Navier–Stokes model discussed here is based on the FLUENT software [2], using its user-subroutine interfaces to specify the heterogeneous chemical-reaction mechanism on the channel walls [3]. The FLUENT software implements a finite-volume approach [4]. The boundary-layer equations are cast as a system of DAEs by the method-of-lines approach [5]. These are then solved using the DASSL software [6]. The plug-flow model [7] is also solved using the DASSL software. The chemistry in both the boundary-layer and plug-flow models is handled through CHEMKIN interfaces [8–10]. The models are quite general in the sense that they can accept alternative chemical-reaction mechanisms and flow conditions.

The results reveal that the boundary-layer and Navier–Stokes models are in excellent agreement over a wide range of flow conditions. The plug-flow model, however, must be used with caution. Under some flow conditions, where the catalytic reaction is mass-transfer limited, the plug-flow model significantly overpredicts the conversion rates. The Navier–Stokes model can take as long as a few hours to converge to a solution, depending on how the iteration is begun. The boundary-layer model, which uses a single-pass marching algorithm from inlet to outlet, produces a solution in a few minutes on a workstation. The plug-flow models require only a few seconds of computation time, but the range of applicability is limited.

2. The single-channel model problem

Fig. 1 shows a typical monolith structure and the particular single-channel geometry used in this study. Since every channel within the monolith structure behaves essentially alike, only one channel needs to be analyzed. Also, a cylindrical channel is used to approximate the actual shape of the channels.

A model problem forms the basis for quantitative comparison of three modeling approaches. The problem considers the flow of a 2.91% methane-in-air mixture that enters a single 2 mm diameter 100 mm long cylindrical channel. The channel walls are assumed to be platinum and held at a fixed temperature of $T_w = 1290\,K$, which corresponds to equilibrium flame temperature (constrained enthalpy–pressure chemical equilibrium) for atmospheric pressure and an initial temperature of 600 K. For the Navier–Stokes and boundary-layer models, a 10 mm entry region has been imposed where there is no catalytic activity. Over the latter 5 mm of the entry region, the wall temperature is ramped up linearly from $T_{in} = 600\,K$ to $T_w = 1290\,K$. For the Navier–Stokes and boundary-layer models, the inlet gas enters the channel at a uniform temperature $T_{in} = 600\,K$. The short inert-wall region is used simply to avoid any computational complications associated with the catalyst leading edge coinciding with the inlet boundary conditions. In the plug-flow model, the mean gas temperature is held fixed at the channel wall temperature.

The flow conditions were chosen to represent a range of gas-turbine-combustor conditions, cover-

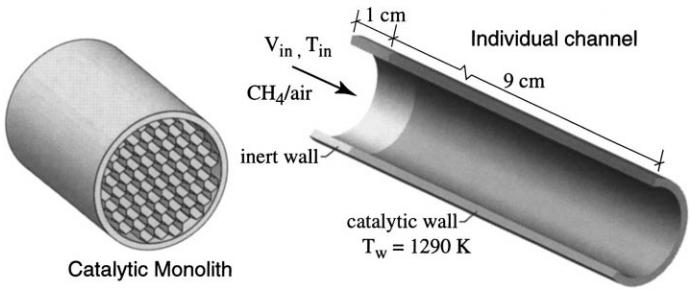

Fig. 1. Illustration of a catalytic honeycomb monolith and an enlarged view of the single-channel model problem. In the model problem, the channel diameter ($d = 2\,mm$) is much smaller than the channel length ($L = 100\,mm$). For clarity, the illustration shows a large channel diameter.

ing a range of physical parameters that include inlet velocities from 0.5 to 5 m/s and pressures from 1 to 10 bar. These conditions can be characterized in terms of a Reynolds number based on channel diameter and inlet flow conditions, which was varied over the range $20 < Re_d = V_{\text{in}} d/\nu < 2000$. The upper limit of $Re_d = 2000$ was chosen to assure laminar flow, hence removing turbulence modeling from the model comparison. While turbulence may have a very important impact on the performance of a catalyst system, it does not affect the conclusions of the model comparison considered here. It should be noted that the validity of the boundary-layer approximations improve as the Reynolds number increases. Thus, at the high Reynolds numbers associated with turbulent flow, a boundary-layer model is especially appropriate. On the other hand, as the Reynolds number decreases, the stream-wise diffusion strengthens relative to the convection. In this case, the accuracy of boundary-layer model can be expected to decrease. A later section of this paper provides a quantitative discussion on the ranges of validity for the three models.

3. The three models

3.1. The Navier–Stokes equations

Beyond assuming perfect-gas behavior, the laminar, multicomponent, chemically reacting Navier–Stokes equations have a few assumptions. Their solution predicts the axisymmetric velocity, pressure, temperature, and species-composition fields in the channel. Mass continuity:

$$\frac{\partial \rho u}{\partial z} + \frac{1}{r}\frac{\partial (r\rho v)}{\partial r} = 0. \tag{1}$$

Axial momentum:

$$\rho u\frac{\partial u}{\partial z} + \rho v\frac{\partial u}{\partial r} = -\frac{\partial p}{\partial z} + \frac{\partial}{\partial z}\left[2\mu\frac{\partial u}{\partial z} - \frac{2}{3}\mu\boldsymbol{\nabla}\cdot\mathbf{V}\right] + \frac{1}{r}\frac{\partial}{\partial r}\left[\mu r\left(\frac{\partial v}{\partial z} + \frac{\partial u}{\partial r}\right)\right]. \tag{2}$$

Radial momentum:

$$\rho u\frac{\partial v}{\partial z} + \rho v\frac{\partial v}{\partial r} = -\frac{\partial p}{\partial r} + \frac{\partial}{\partial z}\left[\mu\left(\frac{\partial v}{\partial z} + \frac{\partial u}{\partial r}\right)\right] + \frac{\partial}{\partial r}\left[2\mu\frac{\partial v}{\partial r} - \frac{2}{3}\mu\boldsymbol{\nabla}\cdot\mathbf{V}\right] + \frac{2\mu}{r}\left[\frac{\partial v}{\partial r} - \frac{v}{r}\right]. \tag{3}$$

Species continuity:

$$\rho u\frac{\partial Y_k}{\partial z} + \rho v\frac{\partial Y_k}{\partial r} = \left(\frac{\partial J_{k,z}}{\partial z} + \frac{1}{r}\frac{\partial (rJ_{k,r})}{\partial r}\right) + \dot{\omega}_k W_k \quad (k = 1, \ldots, K_{\text{g}}). \tag{4}$$

Thermal energy:

$$\rho c_p\left(u\frac{\partial T}{\partial z} + v\frac{\partial T}{\partial r}\right) = \left(u\frac{\partial p}{\partial z} + v\frac{\partial p}{\partial r}\right) + \frac{\partial}{\partial z}\left(\lambda\frac{\partial T}{\partial z}\right) + \frac{\partial}{\partial r}\left(r\lambda\frac{\partial T}{\partial r}\right) - \sum_{k=1}^{K} c_{pk}\left(J_{kz}\frac{\partial T}{\partial z} + J_{kr}\frac{\partial T}{\partial r}\right) - \sum_{k=1}^{K} h_k\dot{\omega}_k W_k. \tag{5}$$

State:

$$p = \frac{\rho RT}{\bar{W}}. \tag{6}$$

In these equations the independent variables are the axial and radial spatial coordinates z and r. The dependent variables are: axial velocity u, radial velocity v, species mass fractions Y_k, temperature T, and pressure p. Other variables are: mass density ρ, viscosity μ, thermal conductivity λ, species enthalpies h_k, and specific heat c_p. The species molecular weights are given as W_k and the mean molecular weight is represented as $\bar{W}$. The diffusive mass flux J that appears in the species conservation equations is discussed subsequently. The gas-phase species production by homogeneous chemical-reaction $\dot{\omega}_k$ is retained in these equations, but it is neglected in the solutions discussed in this paper.

3.2. The boundary-layer equations

The notion of the boundary-layer approximations were first developed in the early 1900s by Ludwig Prandtl, leading to the first practical solution of viscous flow problems. These well-known approximations [11] are applied widely in fluid mechanics. As the

flow rate in the channel increases (i.e., high Reynolds number) the boundary-layer approximations become increasingly valid. Under these circumstances, the axial diffusive transport is diminished in comparison to the radial diffusion and the convective transport. As a result, all the second derivatives in z are eliminated. The radial momentum equation is reduced to the simple statement that there can be no pressure variation across the channel radius. Mathematically, the character of the equations is changed from elliptic to parabolic — a huge simplification, leading to much more efficient computational solution.

Overall mass continuity:

$$\frac{\partial \rho u}{\partial z} + \frac{1}{r}\frac{\partial (r\rho v)}{\partial r} = 0. \tag{7}$$

Axial momentum:

$$\rho u \frac{\partial u}{\partial z} + \rho v \frac{\partial u}{\partial r} = -\frac{\partial p}{\partial z} + \frac{1}{r}\frac{\partial}{\partial r}\left(\mu r \frac{\partial u}{\partial r}\right). \tag{8}$$

Radial momentum:

$$0 = \frac{\partial p}{\partial r}. \tag{9}$$

Species continuity:

$$\rho u \frac{\partial Y_k}{\partial z} + \rho v \frac{\partial Y_k}{\partial r} = \frac{1}{r}\frac{\partial r J_{k,r}}{\partial r} + \dot{\omega}_k W_k \quad (k = 1, \ldots, K_g). \tag{10}$$

Thermal energy:

$$\rho c_p \left(u \frac{\partial T}{\partial z} + v \frac{\partial T}{\partial r}\right) = \frac{\partial}{\partial r}\left(r\lambda \frac{\partial T}{\partial r}\right) - \sum_{k=1}^{K} c_{pk} J_{kr} \frac{\partial T}{\partial r} - \sum_{k=1}^{K} h_k \dot{\omega}_k W_k. \tag{11}$$

The boundary-layer equations form a system of parabolic DAEs, with the time-like direction being the axial coordinate z. They are solved by a method-of-lines procedure, wherein the radial derivatives are discretized using a finite-volume procedure [12,13]. The resulting system of DAEs are solved using the DASSL software [6].

3.3. The plug-flow equations

The plug-flow equations eliminate all diffusive terms. In the axial direction, diffusion is assumed to be small compared to axial convective transport — much the same assumption as in the boundary-layer equations. In the radial direction, however, the diffusive transport (mixing) is assumed to be so dominant that there are no radial variations in the species composition. The plug-flow species-continuity equations are written as

$$\rho u A_c \frac{dY_k}{dz} + Y_k A_s' \sum_{gas} \dot{s}_k W_k = W_k (A_s' \dot{s}_k + A_c \dot{\omega}_k) \quad (k = 1, \ldots, K_g), \tag{12}$$

where $A_c = \pi r_0^2$ is the cross-sectional area of the channel and $A_s' = 2\pi r_0$ is the surface area per unit length (i.e., the channel perimeter). The net mass flow in the channel $\dot{m} = \rho u A_c$ is a constant. Thus, as the species composition changes the density and velocity vary accordingly. Both ρ and u are mean values with no radial variations.

The second term on the left-hand side represents the net mass addition (or depletion) from the gas flow by surface reaction. For a catalytic wall, since there is essentially no net mass exchange, this term vanishes. The terms on the right-hand side represent the production (or depletion) of gas-phase species k by surface ($\dot{s}_k$) and gas-phase ($\dot{\omega}_k$) reaction. For the present model problem, the plug-flow is considered isothermal at the catalyst-wall temperature. Therefore, a thermal energy equation is not needed.

The plug-flow equations, together with the surface chemistry conditions, form a set of DAEs that can be solved along the length of the channel to determine the mean species mass fractions. Here, the system is solved using the PLUG code [7], which is part of the CHEMKIN software package.

3.4. Transport and chemistry

In the above equations, the spatial components of mass flux vector **J** are given as

$$J_{k,z} = -\rho \frac{W_k}{\bar{W}} D_{km} \frac{\partial X_k}{\partial z} - D_k^T \frac{1}{T}\frac{\partial T}{\partial z}, \tag{13}$$

$$J_{k,r} = -\rho \frac{W_k}{\bar{W}} D_{km} \frac{\partial X_k}{\partial r} - D_k^T \frac{1}{T}\frac{\partial T}{\partial r}, \tag{14}$$

where D_{km} are the mixture-averaged diffusion coefficients between species k and the remaining mixture,

D_k^T are the thermal diffusion coefficients, and X_k are the species mole fractions. The diffusion coefficients as well as the thermal conductivity and viscosity, λ and μ, all depend on the local mixture composition and temperature [14]. In the calculations shown here, thermal diffusion has been neglected. However, during the course of the study thermal diffusion was investigated and shown to have a small effect.

The surface reactions produce and deplete both gas-phase species and surface-adsorbed species. The molar production rate of species k by heterogeneous reaction is represented as $\dot{s}_k$. The boundary condition required at the catalyst-wall is that the gas-phase species mass flux produced by heterogeneous chemical-reaction must be balanced by the diffusive flux of that species in the gas

$$\dot{s}_k W_k = J_{k,r} + \rho Y_k v_{\mathrm{st}} \quad (k = 1, \ldots, K_{\mathrm{g}}). \tag{15}$$

This equation serves as an implicit boundary condition from which the gas-phase species mass fractions Y_k at the channel wall are determined. The Stefan velocity v_{st} is the surface-normal fluid velocity that is associated with a net mass exchange at a reacting surface. For the steady-state catalytic processes studied here, the Stefan velocity vanishes. Other boundary conditions at the channel wall are that $u = 0$ and $T = T_{\mathrm{w}}$. At the channel centerline, symmetry is used to specify the required boundary conditions.

The surface reaction mechanism shown in Table 1 was developed by Deutschmann [15–18] and is used in all the simulations in this paper. It consists of 24 heterogeneous reactions, involving seven gas-phase species and 11 surface-adsorbed species. However, the general conclusions of the model-comparison study do not depend on the details of the reaction mechanism.

For the purpose of comparing the three flow models, gas-phase chemistry has been neglected. This is primarily on account of the computational cost and difficulties associated with including large number of gas-phase chemical-reactions in the Navier–Stokes model. As long as there is not a gas-phase combustion ignition, neglecting the gas-phase chemistry has little impact on the general conclusions of the study relative to the validity of the alternative models. A later section of this paper considers the effect of including gas-phase chemistry. The absence of a gas-phase combustion ignition for the honeycomb channel flow parameters used in this paper is verified. However, under circumstances where a gas-phase flame is present and stabilized by upstream diffusive transport, then both of the two reduced models would be seriously in error. Since both reduced models specifically neglect upstream diffusion, essential elements of the stabilization physics are not modeled.

3.5. Discretization and solution

The Navier–Stokes solutions are determined on a nonuniform mesh network having 30 radial elements and 131 axial elements. The radial mesh is concentrated near the channel walls and the axial mesh is clustered near the beginning of the active catalyst. This choice of meshing places the highest mesh concentration in the regions expected to have the largest gradients in the solution. A mesh refinement study confirmed that these choices for meshing lead to mesh-independent results. The honeycomb channel outflow boundary conditions correspond to zero diffusion fluxes for all flow variables in the direction normal to the exit plane.

The boundary-layer calculations use 30 radial mesh points, which are concentrated near the channel walls. The method-of-lines solution procedure automatically picks the axial mesh spacing to assure numerical stability and accuracy. Roughly 300–500 axial mesh points are typical for the calculations reported here. The finest axial meshing occurs near the beginning of the active catalyst, which resolves the high gradients in this region.

The plug-flow model has no radial meshing and the axial step are chosen automatically by DASSL. The axial steps are concentrated near the leading edge of the active catalyst, with a few hundred steps being used overall. The number of steps and their spacing depends on the accuracy requested from the numerical solution.

4. Comparison of the models

A hydrodynamic boundary layer begins to develop immediately as the unreacted flow enters the channel. A thermal boundary-layer begins to grow at $z = 5\,\mathrm{mm}$ as the wall temperature ramps linearly from the inlet temperature of $T_{\mathrm{in}} = 600\,\mathrm{K}$ to the final catalyst-wall temperature of $T_{\mathrm{w}} = 1290\,\mathrm{K}$ at $z = 10\,\mathrm{mm}$. At

Table 1
Reaction mechanism for methane combustion on a Pt surface

	Reaction	A[a]	β[a]	E[a]
(1)	$H_2 + 2Pt(s) \rightarrow 2H(s)$	4.46×10^{10}	0.5	
	The reaction rate is first-order in Pt(s)			
	The reaction has an equivalent sticking coefficient of 0.046			
(2)	$2H(s) \rightarrow H_2 + 2Pt(s)$	3.7×10^{21}		67.4
	The reaction rate is modified by an activated H(s) coverage,[b] i.e.,			
	$k = AT^{\beta}\exp(-E/RT) \times \exp(-\epsilon[H(s)]/RT)$, where the activation parameter $\epsilon = -6$ kJ/mol			
(3)	$H + Pt(s) \rightarrow H(s)$	1.00[c]		
(4)	$O_2 + 2Pt(s) \rightarrow 2O(s)$	1.8×10^{21}	−0.5	
(5)	$O_2 + 2Pt(s) \rightarrow 2O(s)$	0.023[c]		
	Reactions (4) and (5) represent alternative competing pathways			
(6)	$2O(s) \rightarrow O_2 + 2Pt(s)$	1.8×10^{21}		213.2
	The reaction rate is modified by an activated O(s) coverage			
	The activation parameter $\epsilon = -60$ kJ/mol			
(7)	$O + Pt(s) \rightarrow O(s)$	1.0[c]		
(8)	$H_2O + Pt(s) \rightarrow H_2O(s)$	1.0[c]		
(9)	$H_2O(s) \rightarrow H_2O + Pt(s)$	1.0×10^{13}		40.3
(10)	$OH + Pt(s) \rightarrow OH(s)$	1.0[c]		
(11)	$OH(s) \rightarrow OH + Pt(s)$	1.0×10^{13}		192.8
(12)	$H(s) + O(s) \leftrightarrow OH(s) + Pt(s)$	3.7×10^{21}		11.5
(13)	$H(s) + OH(s) \leftrightarrow H_2O(s) + Pt(s)$	3.7×10^{21}		17.4
(14)	$OH(s) + OH(s) \leftrightarrow H_2O(s) + O(s)$	3.7×10^{21}		48.2
(15)	$CO + Pt(s) \rightarrow CO(s)$	1.618×10^{20}	0.5	
	The reaction rate is second order in Pt(s)			
	The reaction is equivalent to a sticking coefficient of 0.84			
(16)	$CO(s) \rightarrow CO + Pt(s)$	1.0×10^{13}		125.5
(17)	$CO_2(s) \rightarrow CO_2 + Pt(s)$	1.0×10^{13}		20.5
(18)	$CO(s) + O(s) \rightarrow CO_2(s) + Pt(s)$	3.7×10^{21}		105.0
(19)	$CH_4 + 2Pt(s) \rightarrow CH_3(s) + H(s)$	4.63×10^{20}	0.5	
	The reaction rate has a 2.3 order dependence on Pt(s)			
	The reaction is equivalent to a sticking coefficient of 0.01			
(20)	$CH_3(s) + Pt(s) \rightarrow CH_2(s)s + H(s)$	3.7×10^{21}		20.0
(21)	$CH_2(s)s + Pt(s) \rightarrow CH(s) + H(s)$	3.7×10^{21}		20.0
(22)	$CH(s) + Pt(s) \rightarrow C(s) + H(s)$	3.7×10^{21}		20.0
(23)	$C(s) + O(s) \rightarrow CO(s) + Pt(s)$	3.7×10^{21}		62.8
(24)	$CO(s) + Pt(s) \rightarrow C(s) + O(s)$	1.0×10^{18}		184.0

[a] Arrhenius parameters for the rate constants written in the form: $k = AT^{\beta}\exp(-E/RT)$. The units of A are given in terms of moles, cubic meters, and seconds. E is in kJ/mol.

[b] The surface coverage (e.g., $[H(s)]$) is specified as a site fraction.

[c] Sticking coefficient. Total available site density for Pt is $\Gamma = 2.7 \times 10^{-9}$ mol/cm^2.

$z = 10$ mm the channel wall becomes catalytically active. The surface chemistry now begins to consume fuel and oxidizer and to release products into the gas. As a result, relatively complex gas-phase species distributions develop.

Figs. 2 and 3 show species contour maps that compare the CH_4 and CO_2 mass fractions from both the Navier–Stokes and boundary-layer models. They are compared at conditions leading to Reynolds numbers of 200 and 2000. The Reynolds numbers ($Re_d = V_{in}d/\nu$) are evaluated using the fluid properties at the inlet conditions. The two models yield results that are in very good agreement. Even at Reynolds numbers as low as 20, the Navier–Stokes and boundary-layer models agree very well.

In each of the contour-plot comparisons, it is apparent that the species contours are a little bit more "spread out" in the Navier–Stokes solutions than in

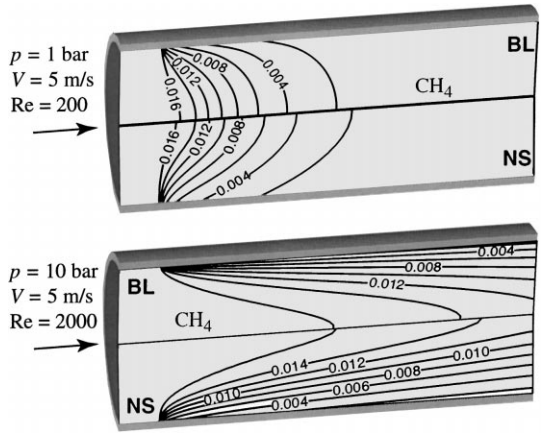

Fig. 2. Comparison of the CH_4 mass fraction contour maps for the Navier–Stokes (lower panels) and boundary-layer (upper panels) models. The upper channel shows $Re_d = 200$ case and the lower channel shows a $Re_d = 2000$ case. For visual clarity, the radial coordinate has been multiplied by a factor of 20. In fact, the channel is much narrower than it appears.

the boundary-layer solutions. This is the anticipated result since the axial diffusive terms are neglected in the boundary-layer equations.

4.1. Mean species profiles

The plug-flow model yields solutions that must be considered as spatially averaged in the radial direction. Thus, to compare plug-flow solutions with

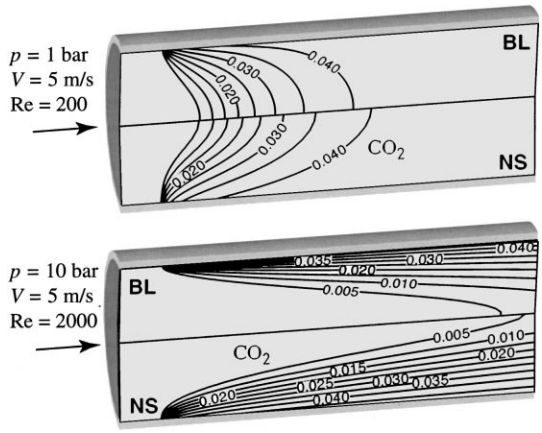

Fig. 3. Comparison of the CO_2 mass fraction contour maps. All other conditions same as in Fig. 2.

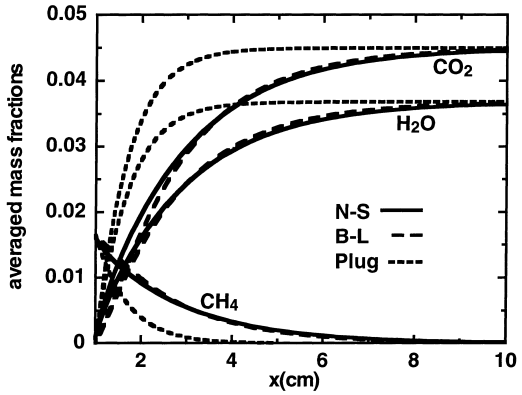

Fig. 4. Axial profiles of the mass-averaged CH_4, H_2O, and CO_2 mass fractions $\bar{Y}_k$ at $Re_d = 200$.

results of the other two models, it is necessary to determine radially averaged species compositions from the Navier–Stokes and boundary-layer solutions. Specifically, at a given axial location, the mass-weighted radially averaged mass fraction can be determined as

$$\bar{Y}_k = \frac{\int_0^{r_0} \rho u Y_k r \, \mathrm{d}r}{\int_0^{r_0} \rho u r \, \mathrm{d}r}. \tag{16}$$

Figs. 4 and 5 show selected axial profiles of major gas-phase species mass fractions for Reynolds number of 200 and 2000. Each figure overlays the results from the three models. In all cases, the plug-flow model predicts a more rapid fuel consumption and creation of products. This is the anticipated behavior, since the inherent radially homogeneous nature of the plug-flow

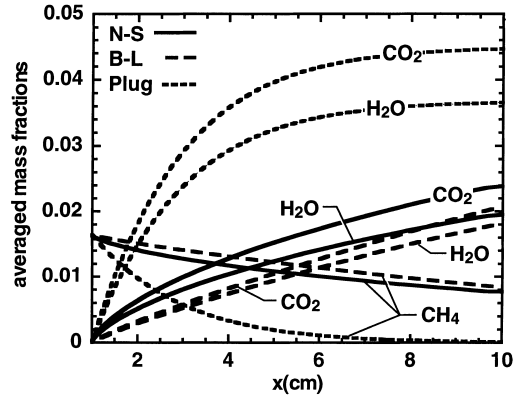

Fig. 5. Axial profiles of the mass-averaged CH_4, H_2O, and CO_2 mass fractions $\bar{Y}_k$ at $Re_d = 2000$.

model imposes more intimate interaction between the gas and the surface. In reality, a species boundary-layer inhibits mass-transfer between the gas and the surface. As discussed in a later section, mass-transfer coefficients can be used to represent the resistance to mass-transfer between the catalytic surface and the mean gas composition.

At $Re_d = 200$ the conversion is nearly complete by the exit of the 100 mm channel. As they must after complete conversion, all three models predict essentially the same major-species composition at the exit. The Navier–Stokes and boundary-layer profiles are essentially indistinguishable. At Reynolds number 2000 (Fig. 5) the plug-flow model again predicts nearly complete conversion by the channel exit. The other two models, however, reveal far less conversion. As seen in the contour maps (Figs. 2 and 3), at high Reynolds number unreacted gas near the centerline penetrates far into the channel. At sufficiently high flow rates, for a given channel dimension, there can be considerable "slip" of unreacted gases exiting the monolith.

Fig. 6 shows mass-averaged CO mass fraction profiles for the three models and at three Reynolds numbers. The Navier–Stokes and boundary-layer models are in good agreement. However, the plug-flow results are in substantial disagreement, with even the functional form of the profiles varying at the high Reynolds numbers. For reasons that will be discussed subsequently, for a fixed-length channel, the plug-flow assumptions become better at lower Reynolds numbers.

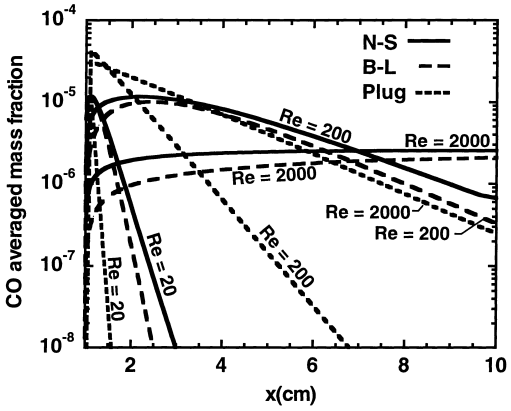

Fig. 6. Axial profiles of the mass-averaged CO mass fractions $\bar{Y}_k$ for Reynolds numbers of 20, 200, and 2000.

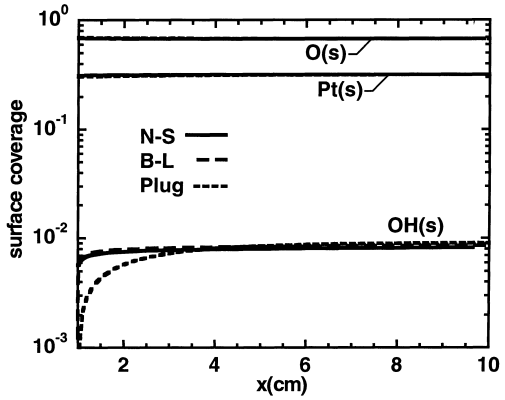

Fig. 7. Comparison of the axial profiles of major-species surface site fractions for the three models. All simulations are at $Re_d = 2000$.

The calculations presented in Fig. 6 have uniformly neglected gas-phase chemistry. Even though the results provide a good comparison of the performance of the three models, it must be noted that homogeneous chemistry has a substantial contribution on the CO profiles. A later section discusses the influence of gas-phase chemistry on the minor-species concentrations and the implications for the three models.

Figs. 7 and 8 show axial profiles of the catalytic-wall surface site fractions for selected surface species at $Re_d = 2000$. The major species, adsorbed oxygen and open platinum sites, are substantially the same

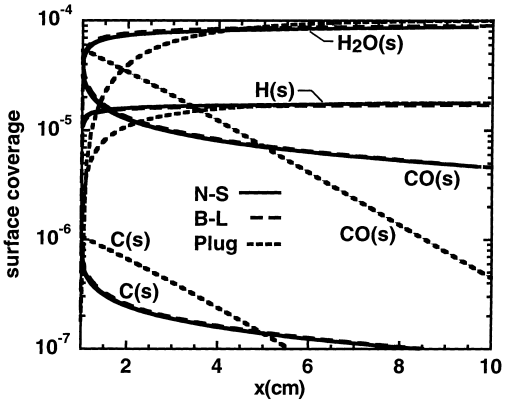

Fig. 8. Comparison of the axial profiles of minor-species surface site fractions for the three models. Surface coverages of CO_2(s) and the three CH_x(s) species are less than 10^{-7}. All simulations are at $Re_d = 2000$.

for all models. The adsorbed OH(s) in the plug-flow model deviates from the other models initially, but quickly comes to the same asymptotic value. Both the Navier–Stokes and boundary-layer models show excellent agreement for the minor surface species. The plug-flow results, however, are substantially different in magnitude and shape for some of these species.

5. Ranges of validity

The validity of the alternative models can be understood in the context of competing time scales for convective and diffusive transport in the axial and radial directions. For flow in a channel, the axial convective time scale can be represented as

$$\tau_{z,\mathrm{C}} \sim \frac{L}{V}, \tag{17}$$

where L is the channel length and V is a characteristic mean fluid velocity. The axial diffusive transport is given as

$$\tau_{z,\mathrm{D}} \sim \frac{L^2}{\mathcal{D}}, \tag{18}$$

where $\mathcal{D}$ is a characteristic diffusion coefficient. The ratio of these two time scales yields

$$\frac{\tau_{z,\mathrm{C}}}{\tau_{z,\mathrm{D}}} \sim \frac{L}{V}\frac{\mathcal{D}}{L^2}\frac{\nu d}{\nu d} = \frac{d}{L}\frac{1}{Re_d Sc}, \tag{19}$$

where d is the channel diameter, ν the kinematic viscosity of the flowing gas, and $Sc = \nu/\mathcal{D}$. (The unity ratio $\nu d/\nu d = 1$ has been introduced to facilitate introduction of the Reynolds and Schmidt numbers.) The underlying assumption in both plug-flow and in boundary-layer flow is that axial diffusive transport over the length scale L is negligible compared to axial convective transport. This implies that $\tau_{z,\mathrm{C}} \ll \tau_{z,\mathrm{D}}$, and hence

$$Re_d Sc\frac{L}{d} = Re_L Sc \gg 1. \tag{20}$$

In the above expression Re_L is the Reynolds number based on the length scale L.

The plug-flow model assumes that there are no radial variations in the solution, i.e., both the radial diffusive and convective transport time scales are much shorter than the axial transport time scales. Moreover, it is safe to assume that the radial diffusive time scales are short compared to radial convective time scales, i.e., diffusion is much more effective than convection in radial mass transport. Thus, since $\tau_{z,\mathrm{C}} \ll \tau_{z,\mathrm{D}}$, it follows that

$$\tau_{r,\mathrm{D}} = \frac{d^2}{\mathcal{D}} \ll \frac{L}{V} = \tau_{z,\mathrm{C}}. \tag{21}$$

Recasting this relationship in terms of dimensionless groups yields

$$\frac{Vd}{\nu}\frac{\nu}{\mathcal{D}} = Re_d Sc \ll \frac{L}{d}. \tag{22}$$

Considering the two plug-flow assumptions together yields practical bounds on range over which the plug-flow assumptions are valid.

$$\frac{d}{L} \ll Re_d Sc \ll \frac{L}{d}. \tag{23}$$

For the specific catalytic-channel problem considered in this paper, $L/d = 100/2 = 50$. Further, for the lean fuel–air mixture $Sc \approx 1$ for most species. Therefore, for the present channel geometry, the plug-flow model should be valid roughly in the range $0.02 \ll Re_d \ll 50$.

It is also interesting to note that the plug-flow model becomes valid again at very high Reynolds numbers where the channel flow becomes fully turbulent, i.e., for $Re_d \gg 2300$. In the fully-turbulent flow regime the characteristic species diffusion coefficient $\mathcal{D}$ in Eqs. (18) and (21) can be replaced by a characteristic turbulent diffusion coefficient $\mathcal{D}_\mathrm{T}$. Following the analysis just described, but replacing the Schmidt number Sc by a turbulent Schmidt number $Sc_\mathrm{T} = \nu_\mathrm{T}/\mathcal{D}_\mathrm{T}$, where ν_T is the turbulent kinematic viscosity, the range of validity of the plug-flow model can be written as

$$\frac{d}{L} \ll Re_d Sc_\mathrm{T}\frac{\nu}{\nu_\mathrm{T}} \ll \frac{L}{d}. \tag{24}$$

The turbulent Schmidt numbers are typically close to unity and the ratio of the turbulent to the laminar kinematic viscosities ν_T/ν scales with the flow Reynolds numbers Re_d [19], yielding a validity range of $0.02Re_d \ll Re_d \ll 50Re_d$ for the plug-flow model. This relationship is always true and hence a plug-flow model is usually valid in the fully-turbulent regime.

The boundary-layer model becomes increasingly valid at high Reynolds number, i.e., $Re_d \gg (d/L)$ or

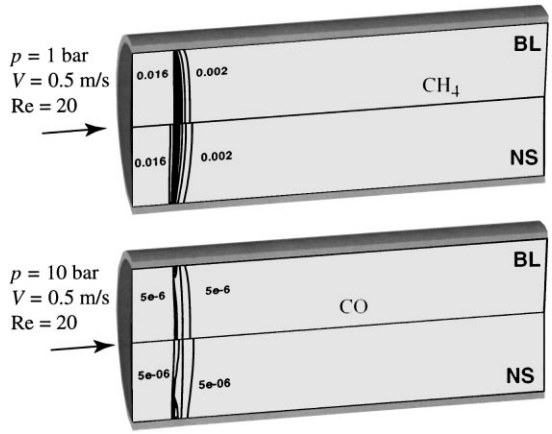

Fig. 9. Comparison of the CH_4 and CO mass fraction contour maps for the Navier–Stokes (lower panels) and boundary-layer (upper panels) models. Both simulations are for $Re_d = 20$. For visual clarity, the radial coordinate has been multiplied by a factor of 20. In fact, the channel is much narrower than it appears.

$Re_L \gg 1$. Some judgement is needed in consideration of the length scale L. Consider the species contours illustrated in Fig. 9 for $Re_d = 20$. If the length scale L is the entire channel length then the entire "combustion event" appears to occur over a very small distance at the leading edge of the catalyst. The contour lines are nearly vertical — just the assumption in the plug-flow model. As viewed over the entire channel length, the Navier–Stokes and boundary-layer solutions are in reasonable agreement, even for a "low" Reynolds number of 20.

If the principal interest is in the details of the solution in the immediate vicinity of the catalyst leading edge, then the axial length scale of interest is very much smaller than the channel length. If the contour plots in Fig. 9 were to be compared over this small region alone, there would appear to be rather large differences between all the models. The plug-flow model would be very bad at this reduced length scale, even though it appears excellent on the scale of the channel length.

At very high Reynolds number the boundary-layer model is likely preferable to the Navier–Stokes model. The assumptions on which it is based are excellent and the computation cost is greatly reduced. Again, judgement is required as to the specific interest in the simulation and the appropriate scales involved. For example, even at very high Reynolds numbers, if the objective is to study the fine details around the leading edge of the catalyst, then the Navier–Stokes models must be used.

All the models are capable of handling gas-phase homogeneous chemical-reactions. However, if gas-phase flame is ignited in the channel, then neither the boundary-layer nor the plug-flow models are appropriate. In this case, the axial diffusive transport is important to the flame-stabilization mechanism. Since the axial diffusion is specifically neglected, then the models do not represent a critically needed physical process.

6. Mass-transfer coefficients

In principle, plug-flow models can incorporate mass-transfer coefficients that improve their accuracy. An underlying assumption in plug-flow models is that the species compositions have only axial variation. Mass-transfer coefficients can be used to approximate the "resistance" to species mass transport between the mean composition and the composition at the reacting channel surface. This approach is especially useful when the mass-transfer coefficients can be determined quantitatively, or reliably estimated, for a range of flow situations. For the complex surface chemistry and the short channels considered here, the mass-transfer coefficients are not easily correlated in a general way. Nevertheless, they can be determined quantitatively from analysis of the boundary-layer or Navier–Stokes solutions.

The mass-transfer coefficients are defined by the following relationship:

$$J_{k,r} = h_k(\rho_{k,\mathrm{s}} - \rho_{k,\mathrm{m}}) = h_k(\rho_{\mathrm{s}} Y_{k,\mathrm{s}} - \rho_{k,\mathrm{m}}) \quad (k = 1, \ldots, K_{\mathrm{g}}), \tag{25}$$

where $J_{k,r}$ is the radial component of the species mass fluxes at the channel wall, h_k the species mass-transfer coefficients, $\rho_{k,\mathrm{s}}$ the species mass densities at the channel surface, $\rho_{k,\mathrm{m}}$ the radially averaged mean species mass densities, ρ_{s} the mixture mass density of the gas at the channel surface, and $Y_{k,\mathrm{s}}$ are the gas-phase species mass fractions at the channel surface.

In general, the mass-transfer coefficients will be different for each species and will vary as a function of

the axial position in the channel $h_k(z)$. Given the full solution for the channel flow field, the mass-transfer coefficients can be determined from

$$h_k = \frac{J_{k,r}}{(\rho_s Y_{k,s} - \rho_{k,m})} = \frac{\dot{s}_k W_k}{(\rho_s Y_{k,s} - \rho_{k,m})} \quad (k = 1, \ldots, K_g). \tag{26}$$

As noted in Eq. (15), at the channel surface the diffusive flux of gas-phase species $J_{k,r}$ is balanced by the production of gas-phase species through heterogeneous reaction $\dot{s}_k$. Since the Navier–Stokes and boundary-layer models compute the surface mass balance, the numerators on the above equations can be easily determined. The radially averaged gas-phase species mass densities are determined from the boundary-layer or Navier–Stokes solutions as

$$\rho_{k,m} = \bar{\rho}\bar{Y}_k \quad (k = 1, \ldots, K_g), \tag{27}$$

where the radially averaged density is calculated from

$$\bar{\rho} = \frac{\int_0^{r_0} \rho r \, dr}{\int_0^{r_0} r \, dr}. \tag{28}$$

In these equations, r_0 is the channel radius, ρ the local gas-phase mass density, $\bar{Y}_k$ the averaged gas-phase species mass fractions as defined in Eq. (16).

The mass-transfer coefficients can be represented in nondimensional form using the species Sherwood numbers

$$Sh_{d,k} = \frac{h_k d}{D_{km}}, \tag{29}$$

where the channel diameter d is used as the length scale. Fig. 10 shows the computed axial profiles of the species Sherwood numbers for three different Reynolds numbers. The abscissa begins at a value of $z = 1$, which is the leading edge of the active catalyst. As expected, the mass-transfer coefficients (Sherwood numbers) have high values at the leading edge and generally decrease downstream toward an asymptotic value of around $Sh_d \approx 3.7$. The high initial values are associated with the very thin mass-transfer boundary layers that begin to develop at the catalyst leading edge. For simple wall boundary conditions, the Sherwood numbers decrease monotonically to an asymptotic value far downstream. For the relatively

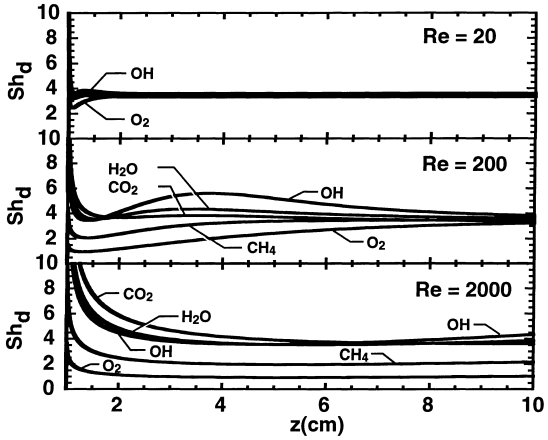

Fig. 10. Axial profiles of selected species Sherwood numbers, $Sh_{d,k} = h_k d/D_{km}$, for three different Reynolds numbers. These profiles were derived from the boundary-layer solutions.

complex heterogeneous chemistry in the catalytic channels, the mass-transfer coefficients evidently do not have simple monotonic behavior.

It is apparent from all the figures that a low Reynolds number flow leads to the active chemistry being confined to a relatively short region in the vicinity of the active catalyst. High Reynolds numbers cause the chemistry behavior to persist farther into the channel. Comparing the Sherwood number behavior in Fig. 10 it is apparent that at $Re_d = 20$, and even $Re_d = 200$, the Sherwood numbers are approaching their asymptotic values by the channel exit. At $Re_d = 2000$, however, the asymptotic values are not achieved within the fixed channel length. When the high Reynolds number calculations are carried much further downstream, the asymptotic values are achieved. These qualitative observations would tend to support the notion that the channel length could be scaled by the Reynolds numbers, leading to more generalized results.

It would be highly desirable to develop generalized correlations between the Sherwood numbers and nondimensional groups that characterize the flow. The mass-transfer equivalent of the so-called Graetz problem [19] would suggest that the Sherwood numbers can be correlated as a function of the species Graetz numbers

$$Gz_k^{-1} = \frac{x/d}{Re_d Sc_k}, \tag{30}$$

where the species Schmidt numbers are given as

$$Sc_k = \frac{\nu}{D_{km}}. \quad (31)$$

In fact, Hayes and Kolaczkowski [20] have previously attempted to determine such correlations for heterogeneous oxidation of methane in a honeycomb monolith channel where a single first-order surface reaction was implemented. The Graetz number correlations can be derived for laminar flow with constant gas-phase composition at the surface or for constant surface reaction rates. In the problem here, neither situation occurs. No general Sherwood number correlations can be found and this finding is consistent with those of the previous study [20]. Nevertheless, beyond the very high values in the immediate vicinity of the leading edge, the Sherwood numbers are all roughly in the range $1 \leq Sh_d \leq 6$.

Assuming that the mass-transfer coefficients can be determined from correlations or simply estimated, their utility is realized only after they are incorporated into the plug-flow simulations. The plug-flow mass-balance equation is still stated as

$$\rho u A_c \frac{dY_k}{dz} + Y_k A_s' \sum_{gas} \dot{s}_k W_k = W_k (A_s' \dot{s}_k + A_c \dot{\omega}_k). \quad (32)$$

However, the surface reaction rate $\dot{s}_k$ is no longer evaluated at the mean mass fraction Y_k, but at the gas-phase mass fraction at the surface. These species mass fractions, $Y_{k,s}$, are determined from

$$h_k(\rho_s Y_{k,s} - \rho_{k,m}) = \dot{s}_k W_k \quad (k = 1, \ldots, K_g). \quad (33)$$

Eq. (33) is an implicit nonlinear algebraic relationship between the heterogeneous reaction rates and the gas-phase composition at the surface. It must be solved simultaneously with the mass-continuity equation, Eq. (32). It is relatively straightforward to implement such an algorithm into a differential-algebraic solver such as DASSL.

7. Effect of gas-phase chemistry

To study the effect of gas-phase chemical reactions, the GRI mechanism, version 1.2 [21], was incorporated into the boundary-layer model. The mechanism considers 32 gas-phase species and 177 reactions.

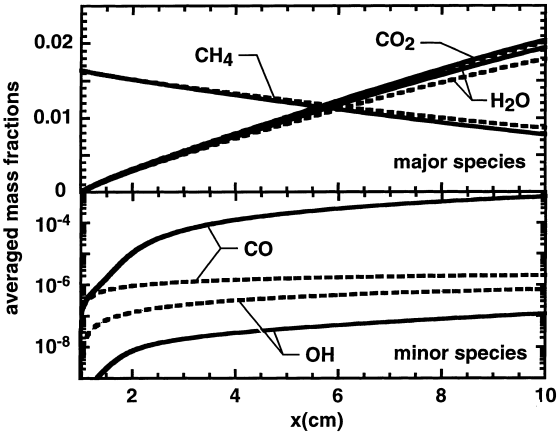

Fig. 11. Comparison of mass-averaged mass fractions of gas-phase species for boundary-layer calculations with and without gas-phase chemistry. Flow conditions correspond to the $Re_d = 2000$ case. Solid curves are for calculation with gas chemistry and broken lines are for calculation without gas chemistry.

Fig. 11 shows results for the Re_d=2000 case, comparing the mass-averaged mass fractions of important gas-phase species, with and without the gas-phase chemistry. Clearly, the gas-phase chemistry plays a relatively small role in determining the concentration of the major species, i.e., CH_4, CO_2, and H_2O. The consumption of CH_4 and the production of CO_2 and H_2O are largely controlled by the surface chemical behavior. However, concentration of the minor species, e.g., OH and CO, is controlled mainly by the gas-phase chemical behavior. Excluding gas chemistry results in serious underprediction of the CO mass fraction and overprediction of the OH mass fraction. However, it is clear that no gas-phase combustion ignition occurs for these conditions.

Fig. 12 compares the surface chemical state for the same boundary-layer calculation with and without gas-phase chemistry. The site fractions of most surface species are virtually independent of whether or not gas-phase chemistry is included in the calculations. For surface species that exist in very low concentrations, such as adsorbed carbon, C(s), differences are seen between the two calculation results.

Overall, the general conclusions drawn from the previous calculations, that compare the three alternative flow models, are not affected by inclusion of gas-phase chemistry. However, caution must be exercised when inferring the behavior of minor species in

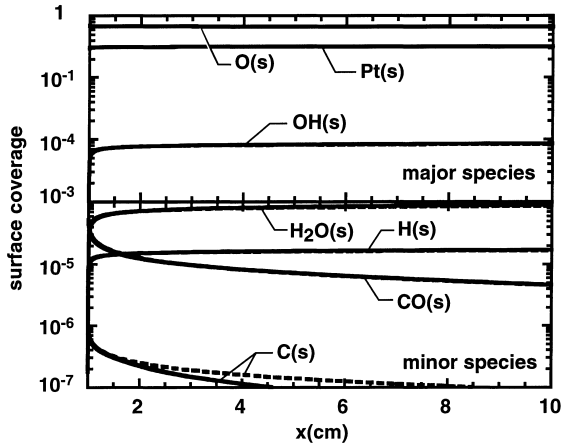

Fig. 12. Comparison of surface species site fractions for boundary-layer calculations with and without gas-phase chemistry. Flow conditions correspond to the $Re_d = 2000$ case. Solid curves are for calculation with gas chemistry and broken lines are for calculation without gas chemistry.

the gas since gas-phase chemistry plays a dominant role in determining their concentrations.

8. Conclusions

Three alternate models for the flow and heterogeneous chemistry in a catalytic channel have been developed and compared for a range of conditions typical of catalytic-combustion monoliths. The range of validity for these models can be established by comparing solutions of a model problem. The validity ranges can also be estimated by consideration of competing time scales. The Navier–Stokes models have very few assumptions and are thus valid in the most general setting. However, they are computationally expensive. For moderate to high Reynolds numbers, the boundary-layer models provide accurate results at much lower computational cost. Plug-flow models are computationally inexpensive, but their range of validity is limited. Mass-transfer coefficients can potentially extend the applicability of plug-flow models, although there appears to be no simple quantitative correlation to determine them. The presence of homogenous reaction has only a small effect on the prediction of major species concentration in the gas-phase. Concentration of minor species in the gas are primarily determined by the gas-chemical behavior. The surface site fractions of most surface species are independent of homogenous chemical reactions.

Acknowledgements

At the Colorado School of Mines, this work was supported by NASA through the CCACS program. O.D. gratefully acknowledges a grant from Deutsche Forshungsgemeinschaft (DFG) for a one-year visit at the University of Minnesota.

References

[1] R.A. Dalla Betta, Catal. Today 35 (1997) 129.
[2] Fluent Version 4.4, Fluent Inc., Lebanon, New Hampshire, 1997.
[3] O. Deutschmann, L.D. Schmidt, AIChE J. 44 (1998) 2465.
[4] S.V. Patankar, Numerical Heat Transfer and Fluid Flow, McGraw-Hill, New York, 1980.
[5] U.M. Ascher, L.R. Petzold, Computer Methods for Ordinary Differential Equations and Differential-algebraic Equations, SIAM, Philadelphia, PA, 1998.
[6] K.E. Brenan, S.L. Campbell, L.R. Petzold, Numerical Solution of Initial-value Problems in Differential-algebraic Equations, 2nd Edition, SIAM, Philadelphia, PA, 1996.
[7] R.S. Larson, Sandia Report SAND96-8211, Sandia National Laboratories, New Mexico, 1996.
[8] M.E. Coltrin, R.J. Kee, F.M. Rupley, Int. J. Chem. Kinet. 23 (1991) 1111.
[9] R.J. Kee, F.M. Rupley, E. Meeks, J.M. Miller, Sandia Report SAND96-8216, Sandia National Laboratories, New Mexico, 1996.
[10] M.E. Coltrin, R.J. Kee, F.M. Rupley, E. Meeks, Sandia Report SAND96-8217, Sandia National Laboratories, New Mexico, 1996.
[11] H. Schlichting, Boundary-layer Theory, 6th Edition, McGraw-Hill, New York, 1968.
[12] M.E. Coltrin, R.J. Kee, J.A. Miller, J. Electrochem. Soc. 133 (6) (1986) 1206.
[13] M.E. Coltrin, H.K. Moffat, R.J. Kee, F.M. Rupley, Sandia Report SAND93-0478, Sandia National Laboratories, New Mexico, 1993.
[14] R.J. Kee, G. Dixon-Lewis, J. Warnatz, M.E. Coltrin, J.A. Miller, Sandia Report SAND86-8246, Sandia National Laboratories, New Mexico, 1986.
[15] O. Deutschmann, F. Behrendt, J. Warnatz, Catal. Today 21 (1994) 461.
[16] O. Deutschmann, Modellierung von Reaktionen an Oberflaechen und Deren Kopplung mit Chemisch Reagierenden Stroemungen, Ph.D. Thesis, University of Heidelberg, 1996.

[17] O. Deutschmann, R. Schmidt, F. Behrendt, J. Warnatz, in: Proceedings of the 26th International Symposium on Combustion, The Combustion Institute, Philadelphia, PA, 1996, p. 1747.
[18] D.A. Hickman, L.D. Schmidt, AIChE J. 39 (1993) 1164.
[19] W.M. Kays, M.E. Crawford, Convective Heat and Mass Transfer, McGraw-Hill, New York, 1980.
[20] R.E. Hayes, S.T. Kolaczkowski, Catal. Today 47 (1999) 295.
[21] M. Frenklach, H. Wang, M. Goldberg, G.P. Smith, D.M. Golden, C.T. Bowman, R.K. Hanson, W.C. Gardiner, V. Lissianski, GRI Report No. GRI-95/0058, 1995.